Supplementary Information: A structure-based model of energy transfer reveals the principles of light harvesting in Photosystem II supercomplexes

Doran I. G. Bennett, Kapil Amarnath, and Graham R. Fleming*

Department of Chemistry, University of California, Berkeley, California

E-mail: fleming@cchem.berkeley.edu

Methods: Extended Description

Energy Transfer Theory

Absorption and Fluorescence: Site Basis

In the limit where all the electronic couplings in a pigment assembly are much weaker than the electron phonon coupling, the absorption/fluorescence spectra of the collective pigment assembly are a sum of the absorption/fluorescence spectra of the individual pigments in a protein bath. The absorption and fluorescence spectra of an individual pigment, given by eqs. (1) and (2), are written in terms of the vertical transition frequency (Ω_μ), line-broadening function $(g_\mu(t))$, and reorganization energy (λ_μ).[1,2] The real-value components of the Fourier transform of eq. (1) and (2) are the frequency domain line shapes of the absorption and fluorescence spectrum, respectively.

$$A_\mu(t) = e^{-i\Omega_\mu t - g_\mu(t)} \tag{1}$$

*To whom correspondence should be addressed

$$F_\mu(t) = e^{-i(\Omega_\mu - 2\lambda_\mu)t - g_\mu^*(t)} \tag{2}$$

$$g_\mu(t) = \int_0^\infty \frac{\mathrm{d}\omega}{\pi\omega^2}\chi_\mu''(\omega)\left[(1-\cos(\omega t))\coth\left(\frac{\omega}{2k_bT}\right) + i(\sin(\omega t) - \omega t)\right] \tag{3}$$

$$\lambda_\mu = \int_0^\infty \frac{\mathrm{d}\omega}{\pi\omega}\chi_\mu''(\omega) \tag{4}$$

The absorption and fluorescence spectra of each pigment are broadened by fluctuations of the phonon environment coupling to the electronic state of the pigments ($H^{\text{el-ph}}$). This influence is incorporated into the line-broadening function $(g_\mu(t))$ through the spectral density $(\chi_\mu''(\omega))$ that describes the distribution of phonon modes as a function of frequency, weighted by their coupling to the electronic structure of the pigment.

Absorption and Fluorescence: Hybrid Basis

In the presence of some delocalization, where the excited states of the pigment assembly can be delocalized across multiple pigments, the absorption and fluorescence spectra are a sum of the absorption/fluorescence spectra of the individual exciton states. The absorption and fluorescence lineshapes, described in the time-domain, are shown in eqs. (5) and (6). Excitonic lineshapes and reorganization energies are linear combinations of pigment functions (eqs. (7) and (8)).[2]

$$A_M(t) = e^{-i\Omega_M t - G_{MMMM}(t)} \tag{5}$$

$$F_M(t) = e^{-i(\Omega_M - 2\Lambda_{MMMM})t - G^*_{MMMM}(t)} \tag{6}$$

$$G_{MNPQ}(t) = \sum_\mu U_{\mu,M}U_{\mu,N}U_{\mu,P}U_{\mu,Q}g_\mu(t) \tag{7}$$

$$\Lambda_{MNPQ} = \sum_\mu U_{\mu,M}U_{\mu,N}U_{\mu,P}U_{\mu,Q}\lambda_\mu(t) \tag{8}$$

Weak Inter-Pigment Electronic Coupling

Energy transfer in the weak electronic coupling limit results from coupling between the transition dipole moments of pigments in different domains (the off-diagonal terms in H^{el} expressed in the

hybrid basis of $|M\rangle$) and can be described by generalized Förster theory[1,2] as shown in eq. (9).

$$k_{M\leftarrow N} = \frac{|V_{M,N}|^2}{\hbar^2 \pi} \int_0^\infty \mathrm{d}t A_M(t) F_N^*(t) \tag{9}$$

$$|V_{M,N}|^2 = |\sum_{\mu,\gamma} U_{\mu,M} H^{\mathrm{el}}_{\mu,\gamma} U_{\gamma,N}|^2 \tag{10}$$

The rate of transfer is proportional to the square of the coupling between the excited states multiplied by the overlap of the fluorescence spectrum of the donor with the absorption spectrum of the acceptor.

Strong Inter-Pigment Coupling

Energy transfer within a domain (because $|M\rangle$ is an eigenstate of H^{el} within the domain) occurs because the electron-phonon coupling drives fluctuations in the site energies of pigments. The changes in the site energy (the diagonal term of H^{el} in the site basis) result in off-diagonal couplings between excitonic states (the change in the Hamiltonian results in $|M\rangle$ no longer being an eigenstate). Phonon driven energy transfer can be described by modified Redfield theory,[2,3] given in eqs. (11)-(12), where the electron-phonon coupling is transformed into the exciton basis and the off-diagonal terms are treated as a perturbation to second-order.

$$k_{M\leftarrow N} = 2\Re \int_0^\infty \mathrm{d}t A_M(t) F_N^*(t) V_{M,N}(t) \tag{11}$$

$$V_{M,N}(t) = e^{2G_{NNMM}(t)+2i\Lambda_{NNMM}(t)} \times \left[\ddot{G}_{NNMM}(t) - \{\dot{G}_{NNNM}(t) - \dot{G}_{NMMM}(t) + 2i\Lambda_{NNNM}\}^2\right] \tag{12}$$

The derivation of eqs. (11) and (12) have been presented previously.[3,4] A concern with using modified Redfield theory is the appearance of negative rates of transfer as the result of numerical instabilities for some inhomogeneous realizations.[3] In the following, if either the up-hill transfer rate or down-hill transfer rate between any pair of excitons was negative, it was replaced with a

rate reconstructed from the other rate of the pair using the detailed-balance criterion. If both rates were negative, the calculation was dropped and a new inhomogeneous realization was selected.

Linearized Kinetics: Effective Forward Transfer Times

The effective forward transfer time ($\tau^{\text{eff}}_{i\leftarrow i+1}$) is the average time for transfer from compartment $i+1$ to compartment i in the presence of the back-transfer away from the final charge separation state (RP2). The effective forward transfer time described in eq. (13) contains two contributions. The first ($k^{-1}_{i\leftarrow i+1}$) can be considered the inverse of the rate of transfer between the $i+1$ and i compartments. The second term, $(1+r_{i+2})$ corrects the forward transfer rate for trajectories that first back-transfer to compartments greater than $i+1$.

$$\tau^{\text{eff}}_{i\leftarrow i+1} = k^{-1}_{i\leftarrow i+1}(1+r_{i+2}) \tag{13}$$

$$k^{-1}_{i\leftarrow i+1} = \sqrt{\langle\sigma_{i-1}|\mathbf{K}_i\mathbf{K}_i^T|\sigma_{i-1}\rangle} \times \frac{\sum_{n\in\text{Domain}}\langle n|\sigma_{i-1}\rangle}{\sum_{n\in\text{Domain}}\langle n|\sigma_i\rangle} \tag{14}$$

$$r_i = -\frac{\sum_{n\in\text{Domain}}^{N_{max}}\langle n|\mathbf{Q}_{i+1}(\mathbf{Q}_{i+1}\mathbf{K}_1\mathbf{Q}_{i+1})^{-1}\mathbf{Q}_{i+1}\mathbf{K}_i|\sigma_i\rangle}{\sum_{n=1}^{N_{max}}\langle n|\sigma_i\rangle} \tag{15}$$

$$\mathbf{Q}_i = \mathbf{I} - \sum_{n=1}^{i-1}|\sigma_n\rangle\langle\sigma_n| \tag{16}$$

Structure and Parameters

Justification of protein structures used

In plants, the photosystem II supercomplex is composed of the reaction center (RC) core surrounded by the Lhcb proteins.[5,6] As shown in Figure 1 of the main text, the core is composed of the two copies each of the proteins RC (composed of D1 and D2), CP43, and CP47, which are all attached to the oxygen evolving machinery. It is difficult to isolate pure, oxygen evolving preparations of the RC core from plants because the oxygen evolving subunits are less stable in

plants, and, as a result, there are no high resolution structures of the RC core from plants.[6] The PSII core from cyanobacteria has generally been used a proxy for the PSII core from plants due to the high similarity in the two protein structures.[7,8] We use a 1.9 Å resolution crystal structure from *Thermosynechococcus vulcanus*, a thermophilic cyanobacterium.[9] The parameters calculated in this paper may be slightly altered if the plant RC core structure is resolved and used instead of the current cyanobacteria structure.

The periphery of the PSII supercomplex is composed of light harvesting complex II (LHCII) trimers. The LHCII trimer structure from plants has been resolved to 2.72 resolution[10] and is used for the calculations in this paper. Between the LHCIIs and the RC core reside the minor LHCs, CP24, CP26, and CP29. No structure has been solved for CP24 and CP26, and no Hamiltonian has been calculated using the structure of CP29. We have substituted an LHCII monomer in place of the three minor LHCs. This substitution is justified for the following reasons. The sequences of the minor LHCs are homologous to those of LHCII and contain nearly all of the binding sites for Chls that LHCII has.[11] Energy transfer within the minor complexes has been shown to have roughly the same dynamics as that in LHCII.[12–14] The CP29 structure shows a high structural homology with the LHCII monomer, though it is missing Chl 605.[15] Trimers of CP26 has been shown to be able to replace LHCII in the protein complex composed of a LHCII trimer, CP24, and CP29 proteins.[16] It has also been suggested that the Lhcb1 protein (one of the proteins in the LHCII trimer) can replace CP24 when it is knocked out in mutant plants, as its expression level goes up by 40% to 60% in such mutants.[17,18] Further refinement in the organization of PSII supercomplexes is unlikely to substantially effect the overall behavior described in this work.

Phototsystem II Parameters

In this section we present the Hamiltonian parameters used to calculate energy transfer in our model. Development of improved Hamiltonians, particularly the availability of better site energies for chlorophyll, could result in changes to our description of energy transfer.

Hamiltonians

Table S1: Transition dipole moment (TDM) magnitudes used to determine Coulombic coupling between pigments associated with different proteins.[14,19]

Protein	Molecule	TDM (Debye)
Reaction Center, CP47, CP43	Chl A	4.4
Reaction Center	Pheophytin	3.5
LHCII, Minor Complexes	Chl A	4.0
LHCII, Minor Complexes	Chl B	3.4

Table S2: Inhomogeneous width of site energies for different molecules in PSII supercomplex.[14,19]

Protein	Molecule	σ (cm^{-1})
Reaction Center	Chl A & Pheophytin	200
Reaction Center	$Chlz_{D1}$	120
CP47	Chl A	180
CP43	Chl A	180
LHCII, Minor Complexes	Chl A	80
LHCII, Minor Complexes	Chl B	96

Table S3: The Hamiltonian for Reaction Center pigments labelled by their common names.[19–21] While there is evidence of a shift in site energies for Chl_{D1} and P_{D1} when the RC is bound in a core complex, we have not included these changes in our Hamiltonian.

P_{D1}	P_{D2}	Chl_{D1}	Chl_{D2}	Pho_{D1}	Pho_{D2}	$ChlZ_{D1}$	$ChlZ_{D2}$
15,015	150	−42	−53	−6	17	1	1
150	15,015	−60	−36	21	−3	1	1
−42	−60	14,750	7	47	−4	3	0
−53	−36	7	14,992	−5	35	0	2
−6	21	47	−5	14,881	3	−4	0
17	−3	−4	35	3	14,815	0	−4
1	1	3	0	−4	0	14,993	0
1	1	0	2	0	−4	0	14,970

Table S4: The Hamiltonian for CP43 pigments labelled by their numbering in the 3arc crystal structure.[22]

CLA 474	CLA 475	CLA 476	CLA 477	CLA 478	CLA 479	CLA 480	CLA 481	CLA 482	CLA 483	CLA 484	CLA 485	CLA 486
14,940	−4	−1	−0.2	−1.6	8.4	8.7	1.3	−5	2.4	−1.1	−0.1	0.3
−4	14,990	−21.9	40.5	0.6	−4.9	−4.4	1.1	11.9	−8.1	7	−4	−0.5
−1	−21.9	14,890	−12.1	−1.3	−0.5	−3	−2.5	−2.3	−9.1	−3.2	10.1	2.1
−0.2	40.5	−12.1	14,760	1.3	2.1	1.3	3.4	−1.4	11.2	1.5	−1.7	1.6
−1.6	0.6	−1.3	1.3	14,840	−7.1	−43.3	−8.2	12	−1.8	−0.4	1.2	−1.9
8.4	−4.9	−0.5	2.1	−7.1	14,990	20	6.7	−15.2	7	2.3	−3.6	4.3
8.7	−4.4	−3	1.3	−43.3	20	14,750	−5.9	40.9	−1.2	−4.3	18.7	−12.7
1.3	1.1	−2.5	3.4	−8.2	6.7	−5.9	14,880	6.1	45.3	22.8	−14.1	5.9
−5	11.9	−2.3	−1.4	12	−15.2	40.9	6.1	14,740	−27.5	63.8	2.3	−2.3
2.4	−8.1	−9.1	11.2	−1.8	7	−1.2	45.3	−27.5	15,140	−41.6	−7.1	4.8
−1.1	7	−3.2	1.5	−0.4	2.3	−4.3	22.8	63.8	−41.6	14,990	−14.4	6.8
−0.1	−4	10.1	−1.7	1.2	−3.6	18.7	−14.1	2.3	−7.1	−14.4	14,950	−31.1
0.3	−0.5	2.1	1.6	−1.9	4.3	−12.7	5.9	−2.3	4.8	6.8	−31.1	15,010

Table S5: The Hamiltonian for CP47 pigments labelled by their numbering in the 3arc crystal structure.[19]

c511	c512	c513	c514	c515	c516	c517	c518	c519	c520	c521	c522	c523	c524	c525	c526
14,684	−49	−12	4	−2	−4	−1	4	−6	−2	−2	3	−2	−1	−2	−1
−49	15,060	−83	20	5	−6	−5	5	−20	−13	−4	6	−9	−2	4	−2
−12	−83	14,793	0	−6	−59	−3	−8	32	15	2	−10	4	−2	−1	−3
4	20	0	14,950	−47	−13	65	5	−11	−6	−1	21	−35	8	−3	0
−2	5	−6	−47	14,810	72	−20	−2	1	−5	−3	−6	−7	−4	13	11
−4	−6	−59	−13	72	14,880	7	−3	8	−4	6	−4	9	4	1	9
−1	−5	−3	65	−20	7	15,130	0	4	1	6	−2	17	3	−2	2
4	5	−8	5	−2	−3	0	14,970	−17	−83	−16	20	−5	−3	3	−1
−6	−20	32	−11	1	8	4	−17	14,810	48	9	−16	10	4	−2	6
−2	−13	15	−6	−5	−4	1	−83	48	15,270	−13	52	0	−6	32	−7
−2	−4	2	−1	−3	6	6	−16	9	−13	14,710	−12	56	37	−18	8
3	6	−10	21	−6	−4	−2	20	−16	52	−12	15,060	−64	95	25	2
−2	−9	4	−35	−7	9	17	−5	10	0	56	−64	14,860	−63	−3	2
−1	−2	−2	8	−4	4	3	−3	4	−6	37	95	−63	14,880	−12	13
−2	4	−1	−3	13	1	−2	3	−2	32	−18	25	−3	−12	14,970	−8
−1	−2	−3	0	11	9	2	−1	6	−7	8	2	2	13	−8	14,530

The LHCII Hamiltonian is exactly reproduced in the SI of Novoderezhkin's work[14] .

Spectral Density

We have used two kinds of spectral densities to define the pigment-protein interaction within the PSII supercomplex. Table S6 shows the spectral density associated with each pigment-protein complex within the system. The equations for both types of spectral densities are given in eqs. (17) and (18). The pigments bound by the core complex are described by eq. (17) using the parameters described in Table S7.[19] The Chl-a and Chl-b pigments bound by LHCII are described by one over-damped Brownian oscillator describing the low-frequency motions of the bath and 48 under-damped Brownian oscillators describing high-frequency intra-molecular vibrations, as shown in eq. (18)[14] . The parameters describing the spectral density used for LHCII pigments are shown in Tables S8 and S9.

Table S6: The spectral density number associated with each pigment-protein complex in PSII.

Protein	Molecule	Spectral Density
Reaction Center	Chl A/Pheophytin	1
CP47	Chl A	1
CP43	Chl A	1
LHCII, Minor Complexes	Chl A	2
LHCII, Minor Complexes	Chl B	2

$$\chi_1''(\omega) = (\pi\hbar)\frac{S_0}{s_1+s_2}\sum_{i=1,2}\frac{s_i(\omega^5)}{7!2\omega_i^4}e^{-\sqrt{\frac{\omega}{\omega_i}}} \tag{17}$$

Table S7: The spectral density parameters that describe core pigments in combination with eq. (17).

Protein	S_0	s_1	s_2	ω_1 (cm^{-1})	ω_2 (cm^{-1})
RC	0.65	0.8	0.5	0.532	1.94
CP47,CP43	0.5	0.8	0.5	0.532	1.94

$$\chi_2''(\omega) = 2\lambda_0 \frac{\omega\Gamma_0}{\omega^2+\Gamma_0^2} + \sum_{j=1}^{N_{\text{vib}}} 2S_j\omega_j^3 \frac{\omega\Gamma_{\text{vib}}}{(\omega_j^2-\omega^2)^2+\omega^2\Gamma_{\text{vib}}^2} \tag{18}$$

Table S8: The spectral density number associated with each pigment-protein complex in PSII.

Protein	Molecule	λ_0 (cm^{-1})	Γ_0 (cm^{-1})
LHCII, Minor Complexes	chl A	37	30
LHCII, Minor Complexes	chl B	48	30

Table S9: The frequencies and Huang-Rhys factors for the under-damped Brownian oscillators describing vibrational modes of Chl A molecules in PSII.

ω_j (cm^{-1})	S_j	ω_j (cm^{-1})	S_j	ω_j (cm^{-1})	S_j
97	$3.95\cdot10^{-2}$	752	$2.1\cdot10^{-2}$	1,286	$3.7\cdot10^{-3}$
138	$4.56\cdot10^{-2}$	795	$3.9\cdot10^{-3}$	1,304	$4.7\cdot10^{-3}$
213	$5.42\cdot10^{-2}$	916	$1.73\cdot10^{-2}$	1,322	$2.47\cdot10^{-2}$
260	$4.44\cdot10^{-2}$	986	$8.4\cdot10^{-3}$	1,338	$3.2\cdot10^{-3}$
298	$3.58\cdot10^{-2}$	995	$1.85\cdot10^{-2}$	1,354	$4.7\cdot10^{-3}$
342	$5.92\cdot10^{-2}$	1,052	$9.9\cdot10^{-3}$	1,382	$5.4\cdot10^{-3}$
388	$2.71\cdot10^{-2}$	1,069	$5.2\cdot10^{-3}$	1,439	$5.4\cdot10^{-3}$
425	$1.73\cdot10^{-2}$	1,110	$9.1\cdot10^{-3}$	1,487	$6.4\cdot10^{-3}$
518	$3.21\cdot10^{-2}$	1,143	$3.33\cdot10^{-2}$	1,524	$5.2\cdot10^{-3}$
546	$2.2\cdot10^{-3}$	1,181	$1.43\cdot10^{-2}$	1,537	$1.78\cdot10^{-2}$
573	$6.9\cdot10^{-3}$	1,190	$5.4\cdot10^{-3}$	1,553	$7.4\cdot10^{-3}$
585	$2.5\cdot10^{-3}$	1,208	$1.5\cdot10^{-2}$	1,573	$3.7\cdot10^{-3}$
604	$1.6\cdot10^{-3}$	1,216	$1.43\cdot10^{-2}$	1,580	$3.7\cdot10^{-3}$
700	$1.6\cdot10^{-3}$	1,235	$5.7\cdot10^{-3}$	1,612	$3.7\cdot10^{-3}$
722	$3.2\cdot10^{-3}$	1,252	$5.2\cdot10^{-3}$	1,645	$3\cdot10^{-3}$
742	$3.21\cdot10^{-2}$	1,260	$5.2\cdot10^{-3}$	1,673	$8\cdot10^{-4}$

Testing Infinitely Fast Intra-Domain Equilibration

In order to assess the reliability of assuming infinitely fast equilibration within domains we calculate the population as a function of time for each domain of the system (the sum of the excitonic populations associated with the domain) with both the full generalized Förster/modified Redfield rate matrix and the domain model that assumes infinitely fast thermalization within each domain.

For each domains population curve as a function of time, we calculate the maximum absolute difference in population between the two methods as a fraction of the maximum population calculated with the full rate matrix (as shown in eq. (19), where d is the index of the domain). This results in no more than 2% error ($\Delta^{(d)}_{\text{max}} \leq 0.02$) no matter which domain is initially excited. We can also characterize the total error over the coarse of a calculation by comparing the integral of the error to the integral of the population curve (as shown in eq. (20)). The integrated error fraction shows less than 7% error ($\Delta^{(d)}_{\text{Integral}} < 0.07$) no matter what domain is initially excited. Figure S1 plots the population curve that has both the largest maximum error and the largest integrated error.

$$\Delta^{(d)}_{\text{max}} = \max\left(\frac{|P^{(d)}_{\text{exc}}(t) - P^{(d)}_{\text{dom}}(t)|}{\max P^{(d)}_{\text{exc}}(t)}\right) \tag{19}$$

$$\Delta^{(d)}_{\text{Integral}} = \frac{\int_0^\infty |P^{(d)}_{\text{exc}}(t) - P^{(d)}_{\text{dom}}(t)|\mathrm{d}t}{\int_0^\infty P^{(d)}_{\text{exc}}(t)\mathrm{d}t} \tag{20}$$

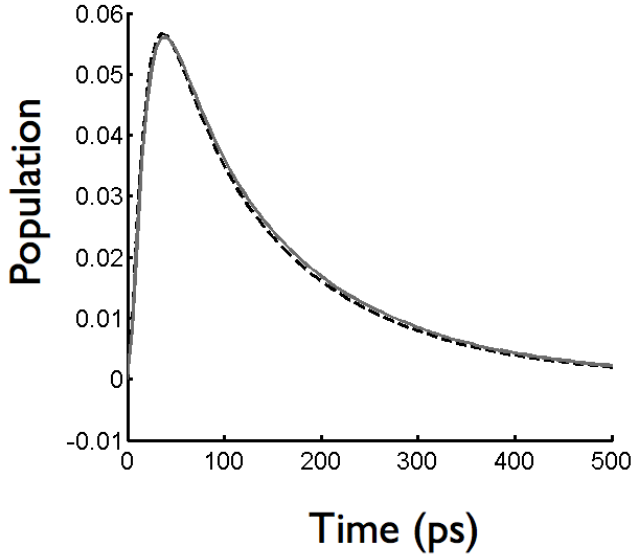

Figure S1: A comparison between the domain population curves with the largest value $\Delta^{(d)}_{\text{max}}$ and $\Delta^{(d)}_{\text{Integral}}$. Population trace calculated with the generalized Förster/modified Redfield (Domain) model is shown with a dashed black (sold grey) line.

Coarse Grained Models of Energy Transfer

The coarse-grain descriptions of energy transfer are calculated by grouping collections of domains into compartments and calculating the Boltzmann-averaged rate constants for transfer between each compartment, as described in the Materials and Methods. Figure S2 (A)-(C) show the timescales of transfer between compartments for the $C_2S_2M_2$ using the protein, transfer-to-trap limited, and trap limited models, respectively. Time constants for energy moving closer (farther) to the final photochemical product RP2 are shown in black (red). When only a single number is shown for a connection, the rates of forward and backward transfer are symmetric. Where no line is shown between proteins, energy transfer timescales were found to be longer than 100 ps and were excluded for clarity. Using the coarse-grained rate matrix, the dynamics of initial charge separation were calculated and the resulting RP1 population trace is shown in Fig. S2 (D). As expected from our previous analysis of the temporal structure of energy transfer in $C_2S_2M_2$, the trap-limited model is found to very poorly reproduce the population dynamics as seen by the overestimate of the early-time charge separation. Both the protein and transfer-to-trap limited models qualitatively reproduce the energy transfer dynamics of the $C_2S_2M_2$, but both models still over-estimate the rate at which excitation energy arrives at the RC and performs charge separation.

Sample Preparation and Modeling

The long lifetime components of the fluorescence decay curves between 1.7 ns and 3.3 ns that have been assigned to contamination by disconnected chlorophyll. We have followed the suggestion of Caffarri and coworkers[23] in removing these long lifetime components prior to fitting the experimental data. The long lifetime components of a fluorescence decay curve, however, report on the balance between the rate of irreversible charge separation and charge recombination at the reaction center. Therefore accurately determining the origin of the long time fluorescence decay in the preparations of PSII supercomplexes is essential for accurately modeling electron transfer kinetics.

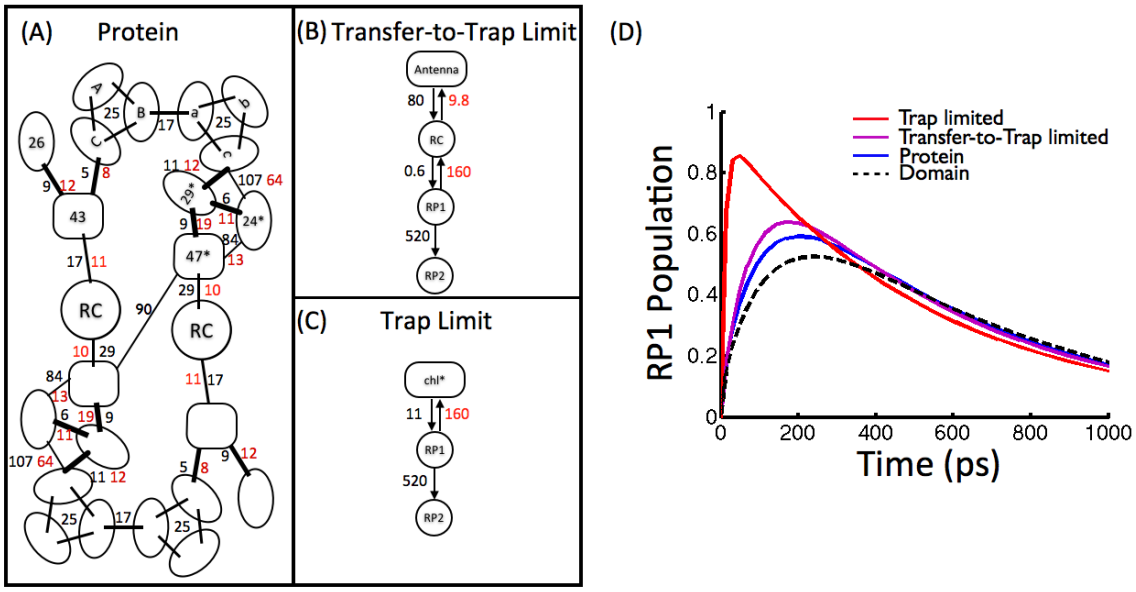

Figure S2: A comparison between different coarse grain models of $C_2S_2M_2$ is shown both as kinetic schemes and simulated RP1 population trace. (A)-(C) The timescales of transfer (k^{-1}) for the various coarse-grain models are shown in units of ps. Numbers in black (red) represent transfers that move excitation closer to (farther away from) the charge separated states. (A)-(C) represent the protein model, transfer-to-trap limited model, and the trap limited model, respectively. (D) The simulated curves for the RP1 population calculated with (τ_{cs} = 0.61 ps, τ_{rc} = 160 ps, and τ_{irr} = 520 ps) are shown in black (Domain), blue (Protein), purple (transfer-to-trap limited), and red (trap limited). The initial excitation was distributed evenly among Chl-a molecules.

Notes and References

(1) Ishizaki, A.; Calhoun, T. R.; Schlau-Cohen, G. S.; Fleming, G. R. *Phys. Chem. Chem. Phys.* **2010**, *12*, 7319.

(2) Novoderezhkin, V. I.; van Grondelle, R. *Phys. Chem. Chem. Phys.* **2010**, *12*, 7352–7365.

(3) Yang, M.; Fleming, G. R. *Chem. Phys.* **2002**, *282*, 163–180.

(4) The equation for $V_{n,m}(t)$ shown in this paper has a different form from that given by Yang and Fleming because we have made use of the additional simplification provided by real valued eigenvectors.

(5) Ballottari, M.; Girardon, J.; Dall'Osto, L.; Bassi, R. *Biochim. Biophys. Acta, Bioenerg.* **2012**, *1817*, 143–157.

(6) Croce, R.; van Amerongen, H. *J. Photochem. Photobiol. B* **2011**, *104*, 142–153.

(7) Buchel, C.; Kuhlbrandt, W. *Photosynth. Res.* **2005**, *85*, 3–13.

(8) Rhee, K.; Morris, E.; Barber, J.; Kühlbrandt, W. *Nature* **1998**, *396*, 283–286.

(9) Umena, Y.; Kawakami, K.; Shen, J.-R.; Kamiya, N. *Nature* **2011**, *473*, 55–60.

(10) Liu, Z.; Yan, H.; Wang, K.; Kuang, T.; Zhang, J.; Gui, L.; An, X.; Chang, W. *Nature* **2004**, *428*, 287–292.

(11) Passarini, F.; Wientjes, E.; Hienerwadel, R.; Croce, R. *J. Biol. Chem.* **2009**, *284*, 29536–46.

(12) Marin, A.; Passarini, F.; Croce, R.; Grondelle, R. V. *Biophys. J.* **2010**, *99*, 4056–4065.

(13) Croce, R.; Müller, M. G.; Caffarri, S.; Bassi, R.; Holzwarth, A. R. *Biophys. J.* **2003**, *84*, 2517–2532.

(14) Novoderezhkin, V.; Marin, A.; Grondelle, R. V. *Phys. Chem. Chem. Phys.* **2011**, *13*, 17093.

(15) Pan, X.; Li, M.; Wan, T.; Wang, L.; Jia, C.; Hou, Z.; Zhao, X.; Zhang, J.; Chang, W. *Nat. Struct. Mol. Biol.* **2011**, *18*, 309–315.

(16) Betterle, N.; Ballottari, M.; Zorzan, S.; de Bianchi, S.; Cazzaniga, S.; Dall'Osto, L.; Morosinotto, T.; Bassi, R. *J. Biol. Chem.* **2009**, *284*, 15255–15266.

(17) de Bianchi, S.; Dall'Osto, L.; Tognon, G.; Morosinotto, T.; Bassi, R. *Plant Cell* **2008**, *20*, 1012–28.

(18)

(19) Raszewski, G.; Renger, T. *J. Am. Chem. Soc.* **2008**, *130*, 4431–4446.

(20) Raszewski, G.; Saenger, W.; Renger, T. *Biophys. J.* **2005**, *88*, 986–98.

(21) Raszewski, G.; Diner, B. A.; Schlodder, E.; Renger, T. *Biophys. J.* **2008**, *95*, 105–19.

(22) Müh, F.; Madjet, M. E.-A.; Renger, T. *Photosynth. Res.* **2012**, *111*, 87–101.

(23) Caffarri, S.; Broess, K.; Croce, R.; van Amerongen, H. *Biophys. J.* **2011**, *100*, 2094–2103.